Electronic Supplementary Material (ESI) for Journal of Materials Chemistry A.

Electronic Supplementary Information for

Electrostatically confined Bi/$Ti_3C_2T_x$ on a sponge as an easily recyclable and durable catalyst for the reductive transformation of nitroarenes

Changqiang Yu[a], Linfen Peng[a], Yisong Zhu[a], Guanshun Xie[a], Zhenjun Wu[b], Xiuqiang Xie*[a], Nan Zhang*[a]

[a]*College of Materials Science and Engineering, Hunan University, Changsha 410082, China*

[b]*College of Chemistry and Chemical Engineering, Hunan University, Changsha 410082, China*

*Corresponding author, E–mail: nanzhang@hnu.edu.cn; xiuqiang_xie@hnu.edu.cn

Contents list

Fig. S16 The photographs of the total (a) Bi–1.0% $Ti_3C_2T_x$ and (b) Bi–1.0% rGO gathered from the resultant solutions after each cycle with the sponge–confined Bi–1.0% $Ti_3C_2T_x$ and sponge–confined Bi–1.0% rGO being successively used for ten times, respectively.

Experimental section

Materials. Titanium aluminum carbide (Ti_3AlC_2) was obtained from Forsman (Beijing) Technology Co, Ltd. Lactic acid ($C_3H_6O_3$), Polyethylene glycol ($H(OCH_2CH_2)_nOH$, M_w=2000), Bismuth ammonium citrate ($C_{12}H_{22}BiN_3O_{14}$), lithium fluoride (LiF), hydrochloric acid (HCl), 3-aminopropyl-triethoxysilane ($C_9H_{23}NO_3Si$, APTES), 4-nitroaniline ($C_6H_6N_2O_2$, 4-NA), 3-nitroaniline ($C_6H_6N_2O_2$, 3-NA), 2-nitroaniline ($C_6H_6N_2O_2$, 2-NA), 4-nitroanisole ($C_7H_7NO_3$), and 4-nitrotoluene ($C_7H_7NO_2$) are obtained from Sinopharm Chemical Reagent Co., Ltd, China. All the reagents are analytical grade and used as received without further purification.

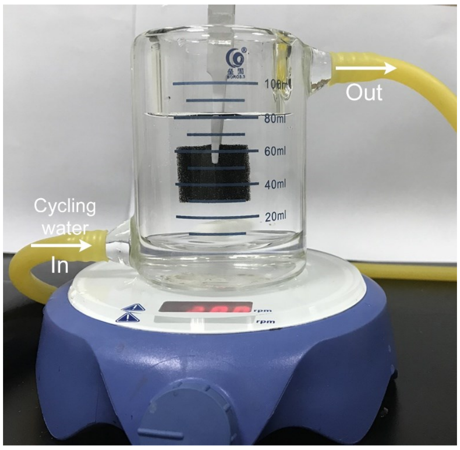

Fig. S1 The photograph of sponge–confined Bi/$Ti_3C_2T_x$ used in catalytic reactions.

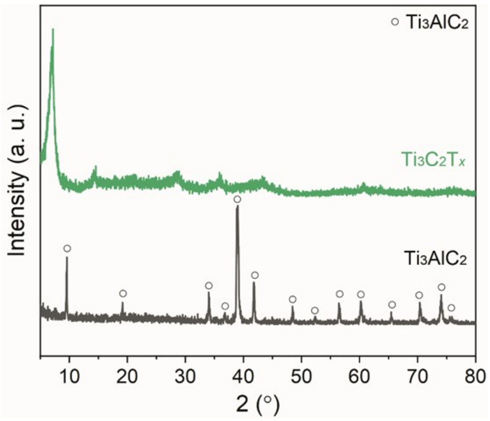

Fig. S2 XRD patterns of Ti_3AlC_2 MAX and $Ti_3C_2T_x$ MXene.

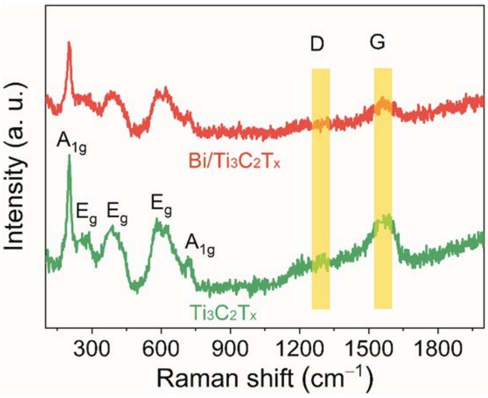

Fig. S3 The Raman spectra of $Ti_3C_2T_x$ and $Bi/Ti_3C_2T_x$.

Supplementary Note: Fig. S3 shows the Raman spectra of $Ti_3C_2T_x$ and $Bi/Ti_3C_2T_x$. The Raman spectra of $Ti_3C_2T_x$ show seven peaks at the range of 200–800 cm^{-1}. Concretely, the A_{1g} out–of–plane vibration modes of Ti and C appear at 203 and 724 cm^{-1}, respectively. Besides, another three bands at 270, 388, and 601 cm^{-1} are be ascribed to the in–plane vibration modes of Ti, C, and the surface functional groups atoms.[S1, 2] The Raman spectra of $Bi/Ti_3C_2T_x$ is identical to that of $Ti_3C_2T_x$, which indicates that $Ti_3C_2T_x$ is stable during the photodeposition of Bi metal. Another two peaks located at 1300 and 1565 cm^{-1} can be ascribed to the D band (signal from the disordered carbon) and G band (signal from the sp^2 hybridized carbon) of carbon species.

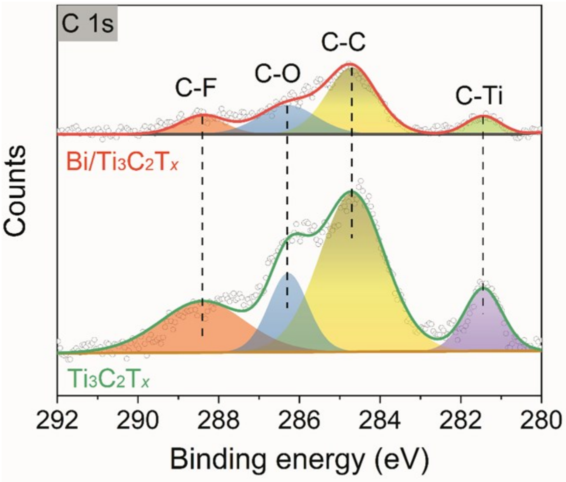

Fig. S4 High–resolution C1s XPS of $Ti_3C_2T_x$ and $Bi/Ti_3C_2T_x$.

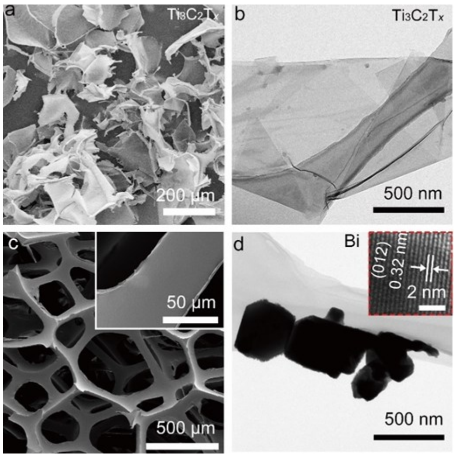

Fig. S5 (a) SEM image and (b) TEM image of $Ti_3C_2T_x$. (c) SEM image of sponge. (d) TEM image of pristine Bi, inset is corresponding high–resolution image.

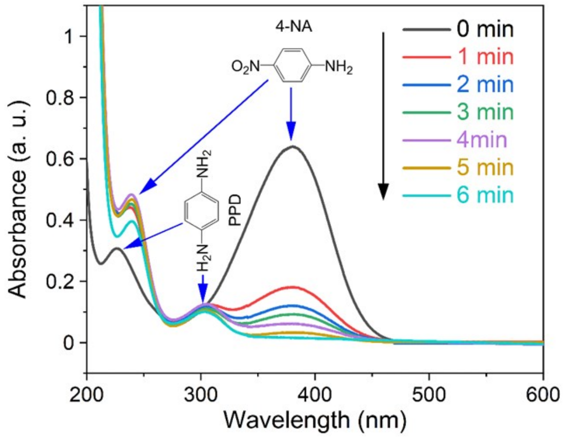

Fig. S6 UV–vis absorption spectra of 4–NA catalyzed by Bi–1.0% $Ti_3C_2T_x$ catalyst.

Table S1 Comparison of the catalytic performances of Bi/$Ti_3C_2T_x$ with those of other catalysts reported in literatures.

Catalysts	*k* (min^{-1})	Catalyst loading	Initial 4–NA	$NaBH_4$	Ref.
Fe_3O_4/Ag	0.45	1.0 mg	2 mL, 5 mM	20 mL, 0.015 M	S3
CuPd	0.33	4.0 mg	20 mL, 0.1 mM	5 mL, 20 mM	S4
Ru/porous carbon	0.01	0.03 mg	40 uL, 0.01 M	160 µL, 0.05 M	S5
AgNPs/T. indica seed coat extract	0.04	0.504 mg	1.5 mL, 1 mM	1.0 mL, 0.05 M	S6
Bi-1.0% $Ti_3C_2T_x$	0.41	1.0 mg	40 mL, 0.07 mM	10 mL, 0.1 M	This work

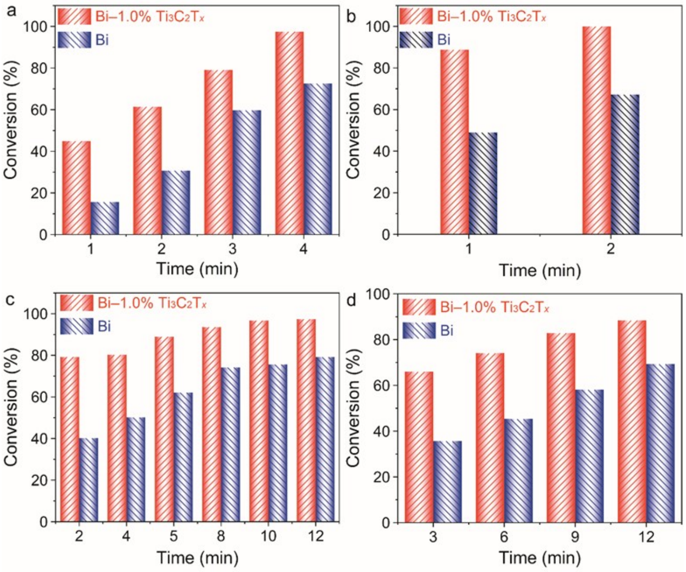

Fig. S7 The conversion (%) of (a) 3–NA, (b) 2–NA, (c) 4–nitroanisole, and (d) 4–nitrotoluene over Bi–1.0% $Ti_3C_2T_x$.

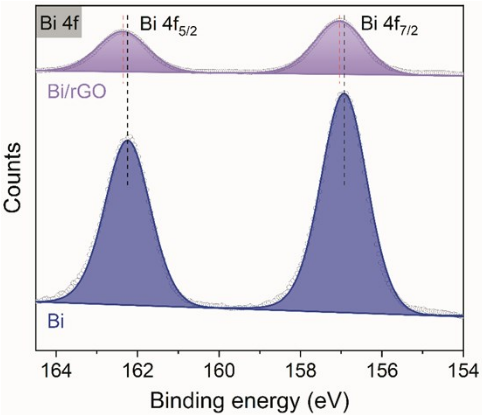

Fig. S8 High–resolution Bi4f XPS of Bi and Bi/rGO.

Supplementary Note: Fig. S8 shows the Bi4f XPS of Bi and Bi/rGO. Two peaks with the binding energies of 162.24 eV and 156.91 eV are assigned to $Bi4f_{5/2}$ and $Bi4f_{7/2}$ of metallic Bi, respectively.[S7] The Bi4f XPS of Bi/rGO shift to higher binding energies compared to pristine metallic Bi, revealing the existance of chemical interaction between Bi and rGO.

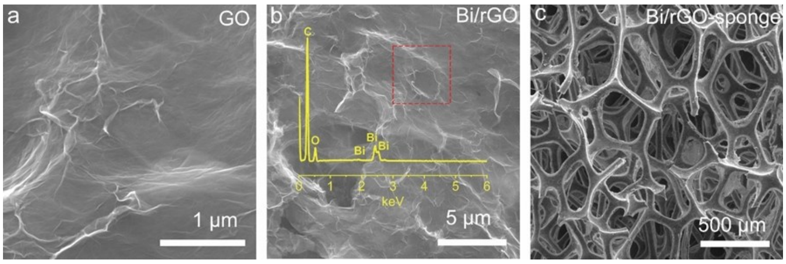

Fig. S9 SEM images of (a) GO, (b) Bi/rGO (inset is EDX spectra), and (c) sponge–confined Bi–1.0% rGO.

Supplementary Note: Judging from Fig. S9a, the surface of GO is wrinkled, which is benneficial to the anchoring of metallic Bi nanoparticles. EDX spectra in Fig. S9b evidently prove the existence of C, O, and Bi elements in Bi/rGO. Combined with XPS analysis (Fig. S8), the growth of Bi on GO is further verified. Fig. S9c corroborates that the electrostatic self–assembly between APTES–mofied sponge and Bi–1.0% rGO is successfully achieved.

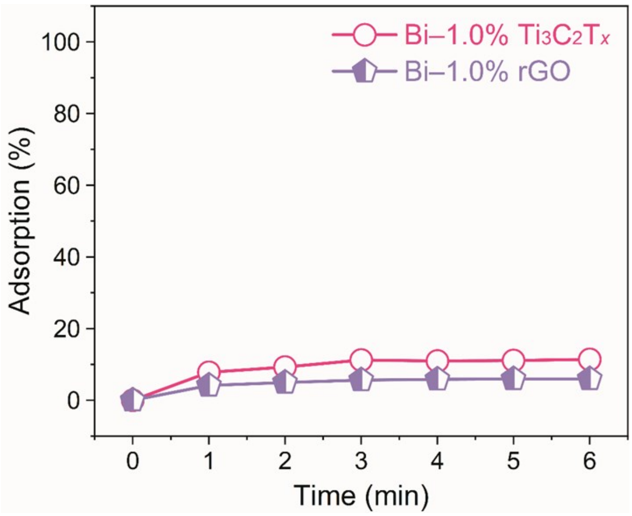

Fig. S10 The adsorption (%) of Bi–1.0% $Ti_3C_2T_x$ and Bi–1.0% rGO for 4–NA.

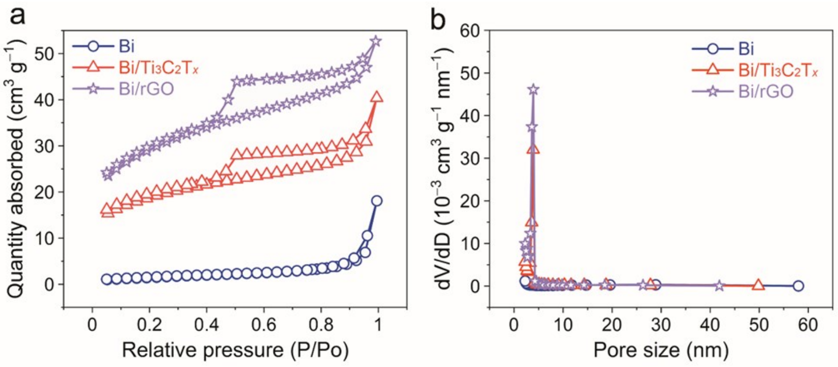

Fig. S11 (a) Nitrogen adsorption–desorption isotherm and (b) Barrett–Joyner–Halenda (BJH) pore size distribution of Bi, Bi–1.0% $Ti_3C_2T_x$, and Bi–1.0% rGO.

Supplementary Note: Fig. S11 shows the surface properties of Bi, Bi–1.0% $Ti_3C_2T_x$, and Bi–1.0% rGO. As shown in Fig. S11a, Bi, Bi–1.0% $Ti_3C_2T_x$, and Bi–1.0% rGO exhibit a type–IV adsorption isotherm, indicating the mesoporous characteristics of the three catalysts. The Brunauer–Emmett–Teller (BET) specific surface area of Bi, Bi–1.0% $Ti_3C_2T_x$, and Bi–1.0% rGO are 5.5 m^2 g^{-1}, 64.2 m^2 g^{-1}, and 100.5 m^2 g^{-1}, respectively. Moreover, the average pore sizes calculated by using BJH for Bi, Bi–1.0% $Ti_3C_2T_x$, and Bi–1.0% rGO are 21.08 nm, 3.16 nm, and 3.03 nm, respectively. Accordingly, the total pore volume of Bi, Bi–1.0% $Ti_3C_2T_x$, and Bi–1.0% rGO are 0.03 cm^3 g^{-1}, 0.04 cm^3 g^{-1}, and 0.05 cm^3 g^{-1}. The calculated parameters as listed in Table S2.

Table S2 The BET specific surface area, average pore size, and total pore volume of Bi, Bi–1.0% $Ti_3C_2T_x$, and Bi–1.0% rGO.

Samples	BET specific surface area ($m^2\ g^{-1}$)	Average pore size (nm)	Pore volume ($cm^3\ g^{-1}$)
Bi	5.5	21.08	0.03
Bi/$Ti_3C_2T_x$	64.2	3.16	0.04
Bi/rGO	100.5	3.03	0.05

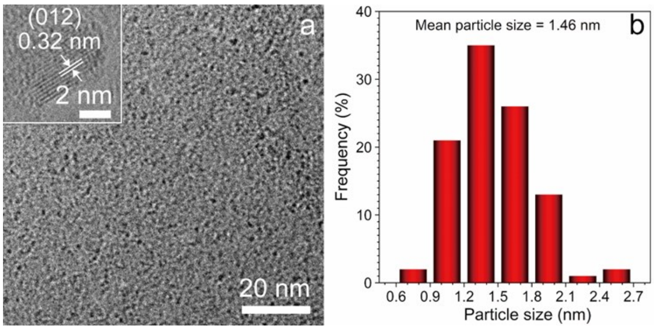

Fig. S12 (a) TEM image of Bi–1.0 % rGO (inset is high–resolution TEM image) and (b) the corresponding particle size distribution of Bi nanoparticles.

Supplementary Note: Fig. S12 shows the TEM image of Bi–1.0% rGO. The lattice fringes of 0.32 nm in the high–resolution TEM image (Fig. S12a) of Bi–1.0% rGO correspond to the *d* spacing of Bi (012) plane. The particle size of Bi nanoparticles anchored on rGO slocates at the range of 0.6–2.7 nm, with the mean particle size of 1.46 nm.

Table S3 The chemical composition of Bi–1.0% $Ti_3C_2T_x$ and Bi–1.0% rGO.

Entry	Ti^a (atom%)	C^b (atom%)	O^a (atom%)	F^a (atom%)	Bi^a (atom%)	Bi^c (wt%)
Bi–1.0% $Ti_3C_2T_x$	26.51	17.67	16.51	11.16	28.15	75.2
Bi–1.0% rGO	–	60.01	27.05	–	12.94	70.6

Note: [a] obtained from XPS analysis; [b] calculated based on XPS and ICP analyses; [c] analyzed by ICP.

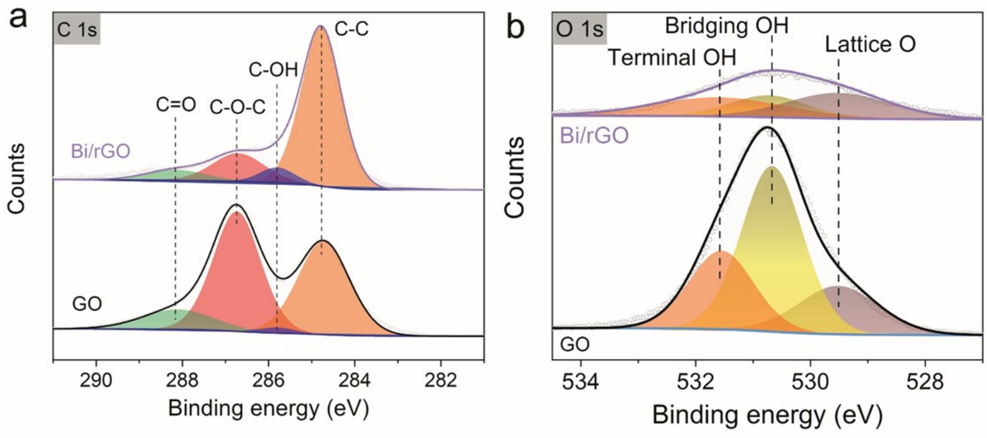

Fig. S13 (a) C1s and (b) O1s XPS of GO and Bi/rGO.

Supplementary Note: Fig. S13 shows the C1s and O1s XPS of GO and Bi/rGO. The fitted four doublets with the binging energies of 288.15 eV, 286.73 eV, 285.80 eV, and 284.77 eV are attributed to C=O, C–O–C, C–OH, and C–C, respectively.[S8-10] The O1s XPS can be fitted into three peaks of lattice O (529.51 eV), bridging OH (530.67 eV), and terminal OH (531.59 eV).[S11, 12] After the photodeposition of Bi, the relative contents of C–C increase from 39.75% to 70.91%, and OH decrease from 38.51% to 20.29%, revealing the reduction of GO.

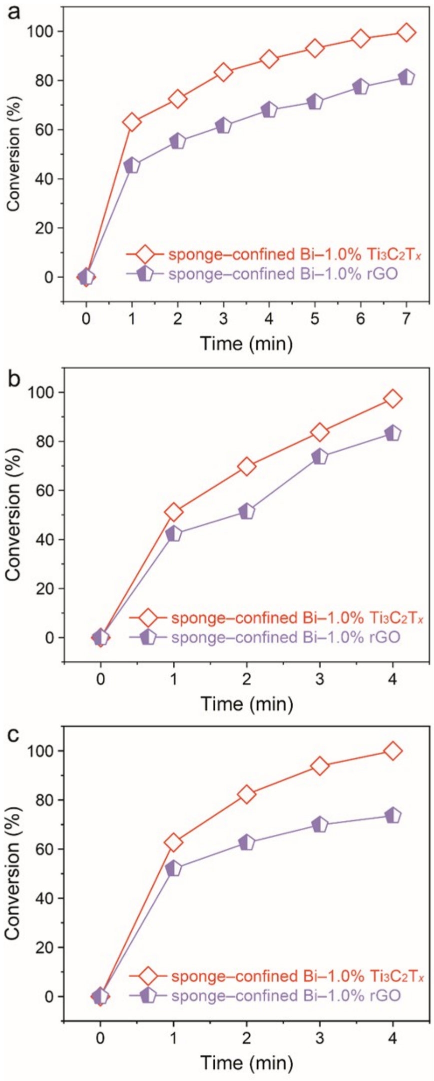

Fig. S14 The conversion (%) of 4–NA, 3–NA, and 2–NA as a function of time over sponge–confined Bi–1.0% $Ti_3C_2T_x$ and Bi–1.0% rGO.

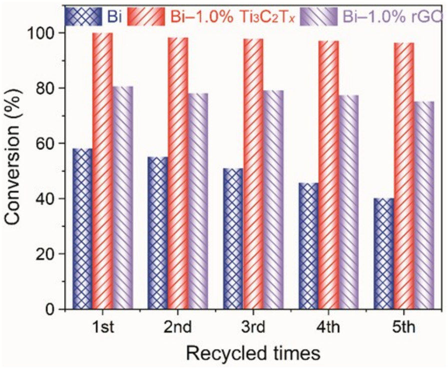

Fig. S15 The successive conversion (%) of 4–NA over Bi, Bi–1.0% $Ti_3C_2T_x$, and Bi–1.0% rGO for five cycles.

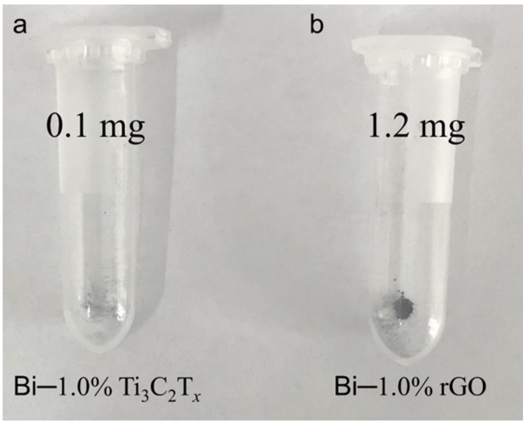

Fig. S16 The photographs of the total (a) Bi–1.0% $Ti_3C_2T_x$ and (b) Bi–1.0% rGO gathered from the resultant solutions after each cycle with the sponge–confined Bi–1.0% $Ti_3C_2T_x$ and sponge–confined Bi–1.0% rGO being successively used for ten times, respectively.

Supplementary Note: Fig. S16 shows the total weights of Bi–1.0% $Ti_3C_2T_x$ and Bi–1.0% rGO collected from the resultant solutions for the sponge–confined Bi–1.0% $Ti_3C_2T_x$ and sponge–confined Bi–1.0% rGO, respectively. The total weight of Bi–1.0% $Ti_3C_2T_x$ (0.1 mg) for the sponge–confined Bi–1.0% $Ti_3C_2T_x$ is lower than that of Bi–1.0% rGO (1.2 mg) for the sponge–confined Bi–1.0% rGO. Thus, it can be concluded that the loss of Bi–1.0% rGO from sponge accounts for the deterioration of catalytic activity.

References

S1. X. Q. Xie, C. Chen, N. Zhang, Z. R. Tang, J. J. Jiang and Y. J. Xu, *Nat. Sustain.*, 2019, **2**, 856-862.

S2. J. Yan, C. E. Ren, K. Maleski, C. B. Hatter, B. Anasori, P. Urbankowski, A. Sarycheva and Y. Gogotsi, *Adv. Funct. Mater.*, 2017, **27**, 1701264.

S3. Y. Xing, X. H. Bai, Y. Gong, M. L. Peng, Y. Y. Zhang, X. R. Ma and Y. Zhang, *J. Magn. Magn. Mater.*, 2020, **510**, 166951.

S4. H. Saikia, B. J. Borah, Y. Yamada and P. Bharali, *J. Colloid Interf. Sci.*, 2017, **486**, 46-57.

S5. S. Y. Feng, M. Ming, M. Z. Wang, X. Wang, D. P. He, P. Jiang and Y. Y. Chen, *Chem. Commun.*, 2020, **56**, 12347-12350.

S6. T. N. J. I. Edison, M. G. Sethuraman and Y. R. Lee, *Res. Chem. Intermediat.*, 2016, **42**, 713-724.

S7. X. W. Li, W. D. Zhang, J. Y. Li, G. M. Jiang, Y. Zhou, S. Lee and F. Dong, *Appl. Catal. B: Environ.*, 2019, **241**, 187-195.

S8. R. Al-Gaashani, A. Najjar, Y. Zakaria, S. Mansour and M. A. Atieh, *Ceram. Int.*, 2019, **45**, 14439-14448.

S9. P. Zhang, T. Song, T. Wang and H. Zeng, *J. Mater. Chem. A*, 2017, **5**, 22772-22781.

S10. K. G. Zhou, K. S. Vasu, C. T. Cherian, M. Neek-Amal, J. C. Zhang, H. Ghorbanfekr-Kalashami, K. Huang, O. P. Marshall, V. G. Kravets, J. Abraham, Y. Su, A. N. Grigorenko, A. Pratt, A. K. Geim, F. M. Peeters, K. S. Novoselov and R. R. Nair, *Nature*, 2018, **559**, 236-+.

S11. C. Q. Li, Y. Huang, X. B. Dong, Z. M. Sun, X. D. Duan, B. X. Ren, S. L. Zheng and D. D. Dionysiou, *Appl. Catal. B: Environ.*, 2019, **247**, 10-23.

S12. C. Q. Yu, M. Wen, S. H. Li, Z. Tong, Y. H. Yin, X. B. Liu, Y. S. Li, Z. P. Wu and D. D. Dionysiou, *J. Hazard. Mater.*, 2020, **398**, 122932.